Chapter 14

Micro-mechanical analysis of failure in advanced composite materials

Conor McCarthy*, Ted Vaughan[1]

Irish Centre for Composites Research, Materials and Surface Science Institute, Department of Mechanical, Aeronautical and Biomedical Engineering, University of Limerick, Ireland.

[1] *Now at the Biomechanics Research Centre (BMEC), Biomedical Engineering, National University of Ireland, Galway.*

Abstract

This chapter sets out to introduce the reader to the important area of micromechanical modelling for the analysis of failure in advanced composite materials. A general introduction to the micromechanical failure in composite laminates is described along with finite element modelling of unidirectional composites to model such failure. The concept of representative volume elements is introduced and statistical methods to characterise composite microstructures are described in detail. A novel approach to recreate statically equivalent microstructure geometries, termed the Nearest Neighbour Algorithm is then developed and used to create advanced 2- and 3- dimensional finite element models. The important concepts of *periodicity* and *homogenisation* are introduced, and then used to extract macroscale elastic moduli. Matrix plasticity and fibre-matrix interface failure models are then introduced and used to predict macroscale strength properties, where extensive material parameter, thermal and cyclic loading studies are carried out. Applications towards modelling macroscale materials and structures are then developed by creating macroscopic failure surfaces and extending the micromechanical models to model composite adhesive joints, where adhesive and composite failure coexist in one single microscale model. Again, extensive parameter studies are carried out. A number of experimental techniques to both calibrate and validate micromechanical models are then described, with some applications. Among the many interesting findings in the chapter, it is shown that while the micromechanical models require a solid understanding of composites, geometric topology, finite element analysis and non-linear material modelling, once they are created they can be used for extensive and cost efficient parameter studies for both composite material design and application to structural features such as bonded joints.

Keywords: Multi-scale modelling, composites, representative volume elements, micro-mechanics, bonded joints, failure analysis

**Corresponding author: conor.mccarthy@ul.ie*

Full Citation: McCarthy, C., and T. Vaughan. "Chapter 14 - Micromechanical Failure Analysis of Advanced Composite Materials." In *Numerical Modelling of Failure in Advanced Composite Materials*, edited by Pedro P. Camanho and Stephen R. Hallett, 379-409: Woodhead Publishing, 2015.

14.1 Introduction

14.1.1 Background

Advanced composite materials are strong, lightweight, engineered materials consisting of high performance reinforcing fibres embedded in a toughened polymeric matrix, to form a *ply* or *lamina*. A suitable number of lamina are then stacked at various orientations relative to each other according to a predefined stacking sequence to form a laminate, as illustrated in Figure 1. The laminate is then formed or reworked to become a structural member for use in high performance systems, such as air and land transport vehicles and renewable energy structures, to name but a few. However, much of their development has been driven by the rapid expansion of the commercial aviation sector, with new generation of efficient aircraft realising composite material usage accounting for upwards of 50% of the airframe structure (by weight). Realising such large composite structures presents a number of challenges, as accurate predictive tools and extensive physical testing are needed in both the design and certification phases of production. Also, the fabrication of such large composite assemblies requires advanced large scale manufacturing and processing techniques.

However, despite the fact that composite materials are being used in primary load-bearing aircraft structures, current design practices and strength predictions are not fully mature and, surprisingly, there is a lack of supporting evidence that many of the ply level failure criteria developed *thus-far* could provide meaningful and accurate predictions for composite materials beyond a limited range of circumstances (Hinton & Soden 1998). Failure in composite materials is a consequence of phenomena taking place at (or below) the microscopic scale and the difficulties associated with accurately predicting material failure is due to the inherent heterogeneity at this scale, i.e. the existence of two phases in the material microstructure with vastly different constitutive behaviour. Local microscopic damage mechanisms, including fibre fracture, fibre-matrix debonding and matrix micro-cracking, contribute to gradual ply degradation. These local phenomenona are rarely independent events as, through the process of damage accumulation, these local failures coalesce and traverse higher length scales until ultimately leading to macroscopic failure.

Thus, failure in an advanced composite is a multiscale process involving the interaction of a multitude of simultaneously occurring local damage mechanisms. This multiscale nature of damage is shown schematically in Figure 1, where damage initiates at the ‘intra-ply level’ through a number of local intra-ply failure mechanisms. At this level, fibre-matrix debonding occurs at the interface and, due to stress redistribution, matrix yielding/cracking occurs in adjoining matrix regions which in turn forms a transverse crack at the ‘ply level’. From the ‘ply level’ the stress concentration at the tip of the transverse crack causes delamination at the ply boundary, as shown, and also results in stress redistribution to neighbouring plies which can bring about earlier failure through fibre fracture, thus affecting the composite on the ‘laminate level’.

Central to the prediction of any multi-scale failure analysis of advanced composite materials and/or structures is the creation and validation of a suitable micromechanical model, and this chapter details the development, validation and utilisation of one such micromechanics model developed by the authors over the past five years (Vaughan & McCarthy 2010; Vaughan & McCarthy 2011a; Vaughan & McCarthy 2011b, McCarthy & Vaughan 2012, Vaughan *et al.* 2012; O’Dwyer *et al.* 2012; O’Dwyer *et al.* 2013; O’Dwyer *et al.* 2014; Hardiman *et al.* 2012).

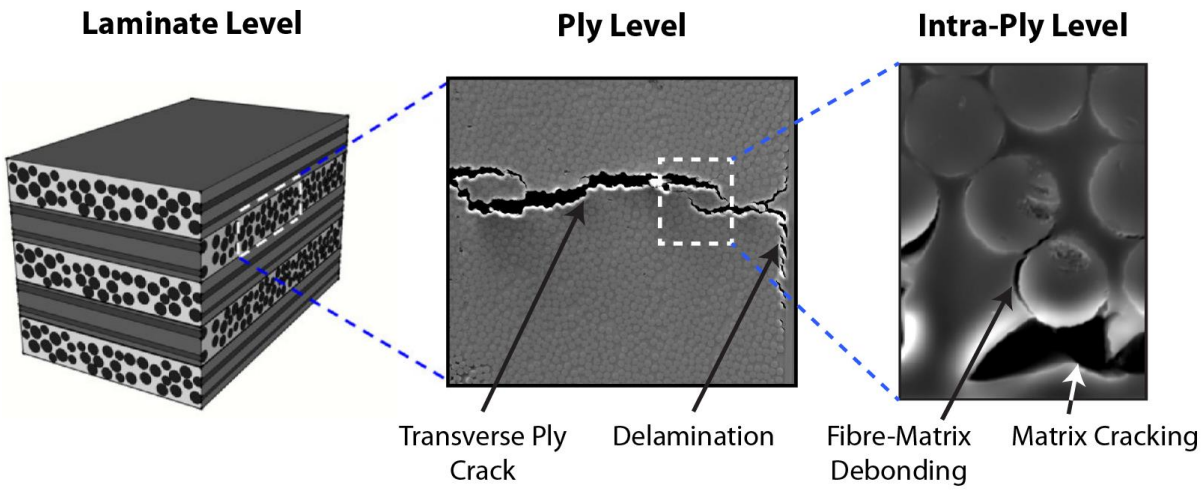

Figure 1: Hierarchical nature of damage in a composite from intra-ply level damage at the microscale to delamination at the macroscale (redrawn using authors own images following Hobbiebrunken et al. *(2006) and Lafarie-Frenot* et al. *(2001))*

14.1.2 Rational

Previously, commercial design practices relied heavily on costly experimental tests on coupons and structural elements, as well as generous safety margins to accommodate material uncertainty. To advance the use of composite materials and maximise their application, predictive capabilities are advancing as an effective means to reduce certification costs as the industry moves towards certification by analysis supported by test and demonstration. The current state-of-the-art in finite element modelling of damage and failure in composite structures uses continuum damage mechanics to predict ply degradation, where various internal damage mechanisms are generalised to create a damage tensor, upon which the mechanical properties depend. While these models allow for an adequate prediction of experimental non-linear behaviour, they still rely on non-physical material parameters, such as plasticity/damage coupling factors, to account for non-linear behaviour (O'Higgins *et al.* 2011). Moreover, these models do not consider the microscopic development of failure and, consequently, offer little insight into *why* composites fail.

Hence, in order to predict microscopic damage accumulation and its effect on the macroscopic structure, multiscale modelling approaches have begun to appear in the literature. In particular, *computational micromechanics* has been shown to provide a suitable framework to present detailed predictions of local deformation mechanisms in heterogeneous materials (González & Llorca 2007). At a fundamental level, any loading situation on composite materials results in an interaction between the constituents, and so representing the fibre and matrix phases discretely in micromechanical simulations facilitates a better understanding of their influence on macroscopic and structural behaviour for both material scientists and engineers. Early computational micromechanics models resolved local stress and strain fields to analyse the effect of particle size, shape and distribution (Brockenbrough *et al.* 1991), thus establishing quantitative relations between the microstructure morphology and physical properties at higher length scales. Recent advances in fracture modelling means discrete microscale damage processes can be simulated through, for example, the use of cohesive zone models at particle interfaces. Llorca, González and co-workers (González & Llorca 2007, Totry et al. 2008, Canal et al. 2009) have combined these with non-linear constitutive models to describe the behaviour of individual phases, providing a computational framework that enables the prediction of diffuse and complex fracture patterns. The work from our group further develops this approach

to better understand the failure behaviour of a carbon fibre/epoxy composite under a range of loading scenarios at both a material and a structural level. This chapter outlines the development of a micromechanics damage model which examines the failure behaviour of a carbon fibre/epoxy composite under a range of loading scenarios at both a material and a structural level.

14.1.3 Current State-of-the-art

The field of micromechanics is extensive and a wide range of strategies are available to predict material behaviour at multiple length scales, including periodic homogenisation models, mean field methods, bounding methods or embedding approaches. Extensive reviews which outline these aforementioned methods have been carried out by Bohm (1998), Trias (2005) and more recently by Pindera *et al.* (2009). In the context of computational micromechanics, the method most widely used is the periodic homogenisation approach.

The accuracy of micromechanics based failure predictions relies heavily upon the definition of a suitable Representative Volume Element (RVE). An RVE normally takes a form similar to that shown in Figure 2, where the fibres of diameter, d_f, are distributed within a square epoxy matrix domain, A, having a side of length, L. The distribution of fibres within the RVE should be statistically equivalent to the actual experimental microstructure (Grufman & Ellyin 2008). A significant number of numerical and experimental strategies have been proposed to define suitable fibre arrangements in the RVE, including the authors' Nearest Neighbour Algorithm (NNA) (Vaughan & McCarthy 2010), which will be used extensively in his chapter.

Indeed, the field of multiscale modelling, and more specifically its implementation using commercial finite element codes, is receiving much attention from academic researchers (Ghosh *et al.* 2007), aircraft manufacturers (de Boer & Poort 2010) and commercial software developers (Firehole Technologies Inc. 2009). The development of such tools can provide widespread access to novel multiscale computational approaches and, consequently, now has commercialisation potential. Indeed, the authors' NNA has also been streamlined into a software tool, and is available for download (McCarthy & Vaughan 2012).

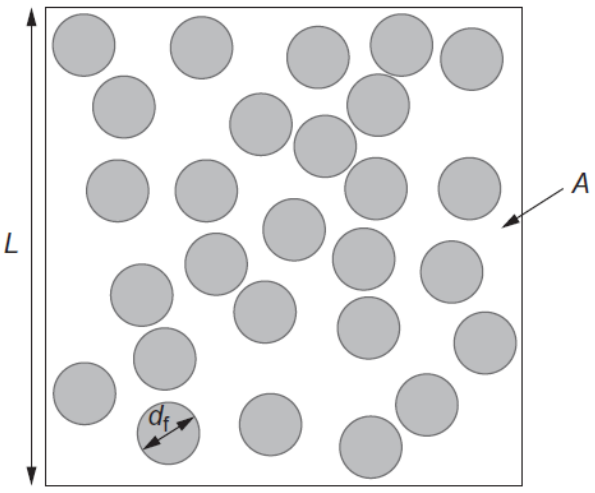

Figure 2: Idealised square RVE

14.1.4 Chapter outline

This chapter begins by examining microstructure generation and characterisation, where real carbon fibre reinforced plastic (CFRP) microstructures are presented. Statistical characterisation of these microstructures is then presented, where a number of important

statistical descriptors are defined and then utilised to create the NNA. The NNA is then used to create statistically equivalent microstructure geometries for input into the finite element models. In Section 3, finite element model development is described. Representative Volume Elements (RVE's) are defined and described along with Periodic Boundary Conditions (PBC's) and non-linear material property modelling. Section 4 describes prediction of mechanical properties for the composite including macroscale modulus and strength predictions. Section 5 is dedicated to micromechanical analysis applications of macroscopic materials and structures, which includes the analysis of bonded composite joints. Micromechanical experimental calibrations and validation techniques are described in Section 6, with some applications. Finally, the chapter closes with conclusions and ways forward, future research topics and some information on related journals and conferences.

14.2. Microstructural Characterisation and Generation

14.2.1 Experimental Characterisation of Composite Microstructures

This section considers the spatial arrangement of fibres in HTA/6376, a high strength CFRP used extensively in the aerospace industry. Transverse sections were prepared for microscopy from a 2 mm thick, 16-ply unidirectional composite laminate using standard grinding and polishing techniques, which used a final particle size of 0.05μm. The analysis considered 40 images from the transverse cross-sections, each measuring 320μm × 240μm and one of these is shown in Figure 3(a). Digital image analysis was used to extract fibre diameters and *x,y* coordinates of each fibre centre, by using a colour threshold in each image, as shown in Figure 3(b).

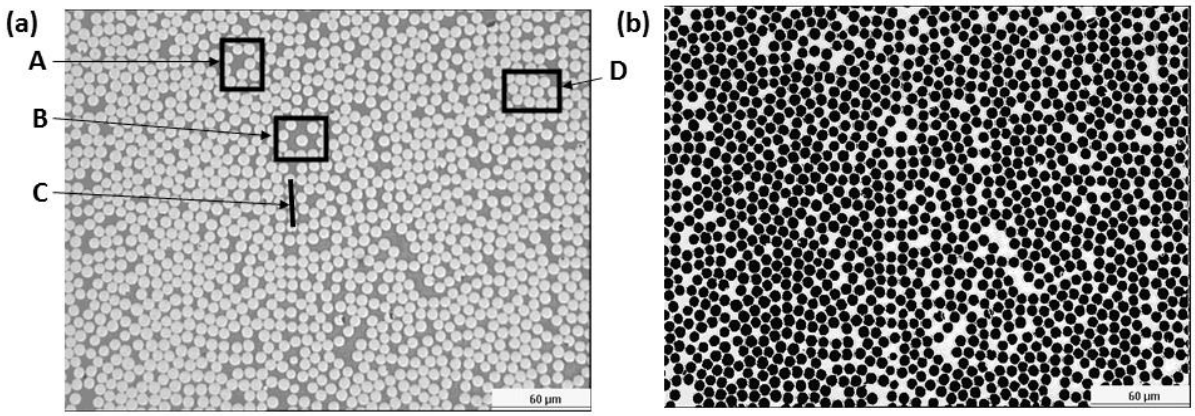

Figure 3: (a) Micrograph of HTA/6376 and, (b) computed microstructure obtained using digital image analysis

14.2.2 Statistical Characterisation of Composite Microstructure

The data extracted from the digital image analysis was used to generate statistical functions that characterise the morphology of the CFRP microstructure. Figure 4(a) shows the distribution of fibre diameters, which conformed to a lognormal distribution, as shown. The mean fibre diameter was 6.6μm and the fibre volume fraction (V_f) was computed as 59.2%. To characterise the spatial arrangement fibres, nearest neighbour distribution, second-order intensity and radial distribution functions are considered to describe both short and long range interactions of fibres, which are discussed below.

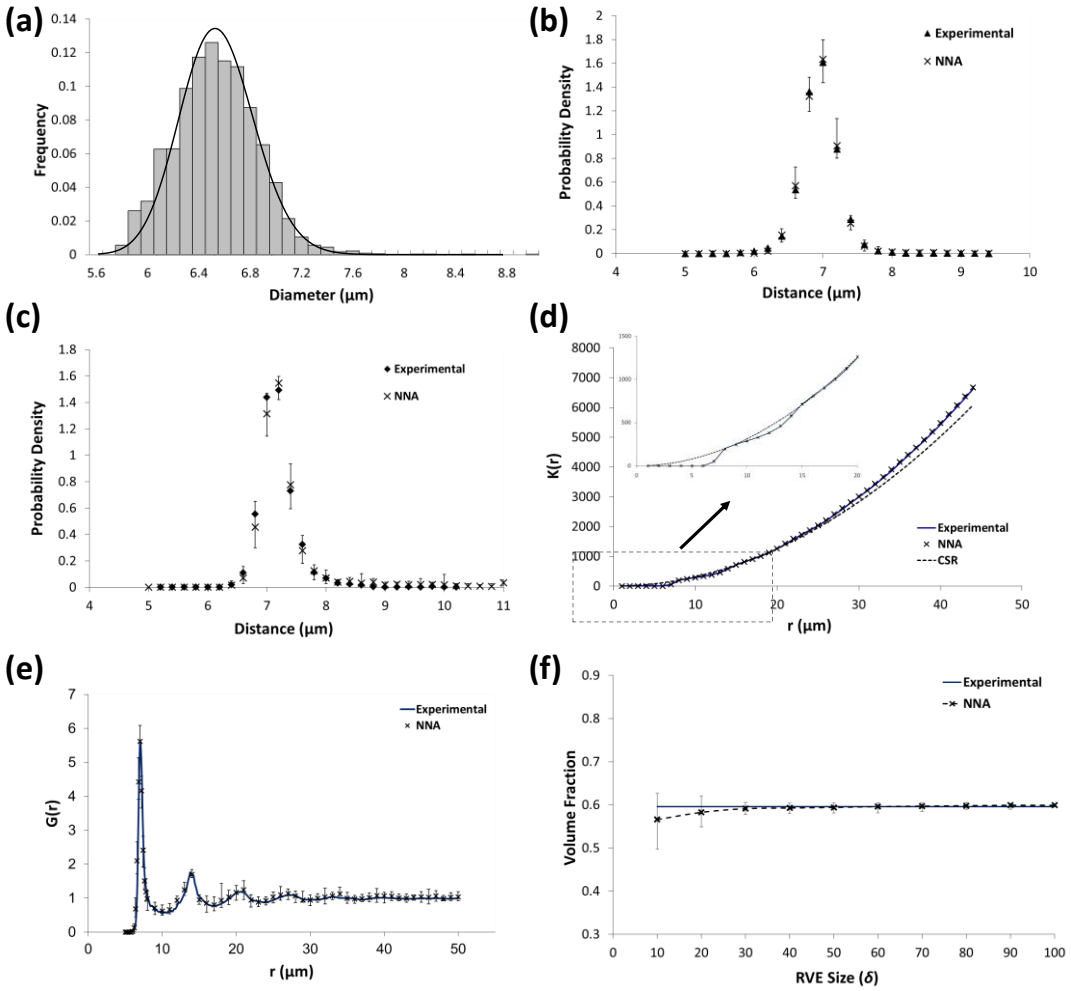

Figure 4: Statistical functions used to characterise both short and long range interactions of fibres within experimental microstructure and numerically generated microstructures (NNA); (a) Fibre diameter distribution fit to a lognormal distribution curve (b) 1st nearest neighbour distribution function, (c) 2nd nearest neighbour distribution function, (d) second-order intensity function, (e) radial distribution function and (f) effect of RVE size on fibre volume fraction

Nearest Neighbour Distribution Functions

Nearest neighbour distribution functions can detail the short range interaction of fibres by analysing the distance between each fibre and their n^{th} closest neighbour (Diggle 2003). Shown respectively in Figures 4(b) and (c) are the *1*st and *2*nd nearest neighbour distributions of fibres. These distributions exhibit narrow ranges, and high peaks occur at distances of 7μm and 7.2μm, respectively. From Figure 4(a), the mean of the diameter distribution was found to be 6.6μm, which implies that, for neighbouring fibres, the average inter-fibre spacing is in the region of 0.4μm-0.6μm.

Second-Order Intensity Functions

The second-order intensity function, *K(r)*, may be used to distinguish between different types of point patterns and is defined as the number of further points expected to lie within a radial distance, *r*, of an arbitrary point (see Figure 3(a)), divided by the number of points per unit area. The boundary of the domain has a significant effect when calculating this function and an estimator which accounts for edge-correction has been established by Ripley (1977) as,

$$K(r) = \frac{A}{N^2} \sum_{k=1}^{N} w_k^{-1} I_k(r) \qquad \textbf{(1)}$$

where N is the total number of points in the area, A. $I_k(r)$ is the number of points lying within a radial distance, r, of a given fibre and w_k is the ratio of the circumference lying within the area, A, to the whole circumference of the circle. Shown in Figure 4(d) are the second-order intensity functions for the CFRP composite and a distribution that exhibits Complete Spatial Randomness (CSR), described by $K(r) = \pi r^2$. It can be seen that the experimental curve is initially below the CSR curve and shows evidence of a slight stair-shape, which is indicative of a certain amount of regularity in the fibre arrangement at shorter distances (i.e. $r \leq 15\mu m$). However, at larger distances (i.e. $r > 15\mu m$) the curve is above and diverging away from the CSR pattern, which is a result of long range clustering.

Radial Distribution Functions

The radial distribution function can describe how the average fibre density varies as a function of distance from a given fibre centre. It is found by determining the number of fibres lying within an annular region of inner radius, r, and outer radius, $r+dr$ (see Figure 3(a)) and dividing this by the average number of fibres per unit area. It is closely related to the derivative of the second order intensity function and is mathematically defined as,

$$G(r) = \frac{1}{N_a (2\pi r)} . \frac{dK(r)}{dr} \qquad \textbf{(2)}$$

where, $dK(r)$ is the average number of fibre centres lying within an annulus of inner radius, r, and outer radius, $r+dr$, and N_a is the number of fibres per unit area. The measured radial distribution function of the CFRP microstructure, shown in Figure 4(e), exhibits a large peak at a distance of 7μm, which coincides with the peak seen in the 1^{st} nearest neighbour distribution function (shown in Figure 4(b)). For the medium range (i.e. $10\mu m \leq r \leq 25\mu m$), the function exhibits some fluctuations, typical of a high volume fraction composite, due to the physical area taken up by the fibres. At the long range (i.e. $r \geq 25\mu m$), the function approaches unity as the value of r becomes large enough to be representative of the overall region, indicating that the microstructure is statistically homogeneous.

14.2.3 Numerical Microstructure Generation

Nearest Neighbour Algorithm

The Nearest Neighbour Algorithm (NNA) was developed to generate high volume fraction fibre distributions that are statistically equivalent to the CFRP microstructure, characterised above. The importance of the short range interaction of fibres has already been highlighted and so, to accurately reproduce this, the NNA uses a bottom-up approach that populates a region

using an *'adjusted'* measure of *1st* and *2nd* nearest neighbour distribution functions (Vaughan & Mccarthy 2010).

1. A random point is created having coordinates (x_1, y_1), lying in a sample square area, *A*. The diameter, d_1, of the surrounding fibre is drawn from a lognormal distribution fitting the experimentally measured diameter distribution, as shown in Figure 4(a).

2. A second point is created (x_2, y_2), which is the centre of the first nearest neighbour of the previous fibre. The distance from (x_1, y_1) to (x_2, y_2) is assigned from the adjusted first nearest neighbour distribution function and the new point is oriented at a random angle θ_1, as shown in Figure 5(a). The fibre diameter is assigned from the experimentally measured diameter distribution, as before.

3. A third point is created (x_3, y_3), which is the centre of the second nearest neighbour of the first fibre. The distance from (x_1, y_1) to (x_3, y_3) is assigned from the adjusted second nearest neighbour distribution function and the new point is oriented at a random angle θ_2, as shown in Figure 5(b), while the fibre diameter is assigned from the experimentally measured diameter distribution.

4. The process is repeated for each fibre thereafter (see Figure 5(c)) until the sample area is filled, as shown in Figure 5(d). The NNA ensures that none of the fibres overlap with one another and the fibres lie within the sample area chosen. If overlaps occur or a fibre is placed outside the sample area, orientation angles or inter-fibre distances are reassigned until a suitable configuration is found. If no suitable configuration can be found (i.e. near a boundary or in a region saturated with fibres), the algorithm will then move on to the next fibre and continue as before. For any fibre crossing a boundary, a corresponding fibre is placed on the opposing boundary to maintain geometric periodicity.

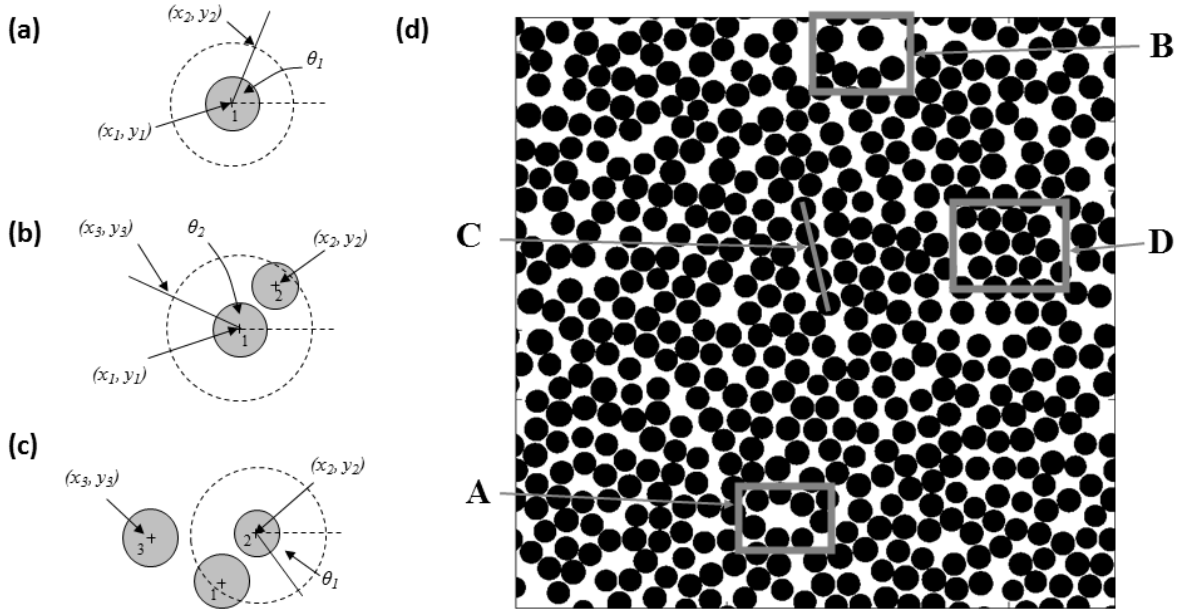

Figure 5: (a) Assigning a fibre's nearest neighbour (b) Assigning a fibre's second nearest neighbour (c) Nearest neighbour being assigned for a subsequent fibre (d) Generated distribution using Nearest Neighbour Algorithm

Statistical Characterisation of Numerical Microstructures

A resulting microstructure measuring 165µm × 165µm is shown in Figure 5(d), where the NNA is seen to reproduce short range regularity, matrix rich regions and 'lines' of fibres much the same as in the original micrograph (compare Figure 3(a) with figure 5(d)). Four regions (A, B, C and D) have been identified in both images to highlight these similarities. A statistical analysis of 20 microstructures generated by the NNA has shown excellent correlation between nearest neighbour, radial and second-order intensity function when compared to the experimentally measured statistical functions, as shown in Figure 4(b)–(e). This shows that the NNA recreates both short and long range interactions of fibres of the original CFRP microstructure.

The effect of RVE size and resulting fibre volume fraction of a series of microstructures generated by the NNA is shown in Figure 4(f), where there is a large variance in resulting V_f for the smallest models, i.e. $\delta = 10$, where δ is defined as the length of the side of the RVE (L) divided by the fibre radius (r_f). This is due to the relative size of the fibres compared to the overall RVE window size and the conditions the NNA uses when placing fibres near a boundary. For smaller models, the influence of the boundary is relatively large compared to the overall area of the RVE. The larger models (i.e. $\delta \geq 20$), are seen to converge close to the experimental fibre volume fraction of 59.2% showing very little variance in the fibre volume fractions being produced.

14.3. Finite Element Framework

14.3.1 Model Description

Microstructural Geometries

For micromechanical analyses, the NNA allows a range of RVEs to be generated that are statistically similar but topologically different. Figures 6(a) and 6(b) show two-dimensional representations generated by the NNA that measured 66×66µm (δ=20) and each containing approximately 80 fibres. These geometries were exported to the ABAQUS finite element code using Python scripts to create two- and three-dimensional finite element models. For the two-dimensional case, fibre and matrix regions were discretised using a quad-dominated mesh, consisting of predominantly 4-noded (CPEG4) and a relatively small number of 3-noded (CPEG3) full integration generalised plane strain elements. A layer of 4-noded cohesive elements (COH2D4) was introduced between the fibre and the matrix to predict the onset of fibre-matrix debonding. In three-dimensions, fibre and matrix regions were discretised using 6-noded wedge elements (C3D6), while eight-noded cohesive elements (COH3D8) were introduced between fibre and matrix regions to predict fibre-matrix debonding. To ensure accurate prediction of shear bands in the matrix, sufficiently dense meshes consisting of approximately 85,000 elements were used. It was found that any increased mesh refinement provided no further accuracy to the solutions obtained (Vaughan 2011).

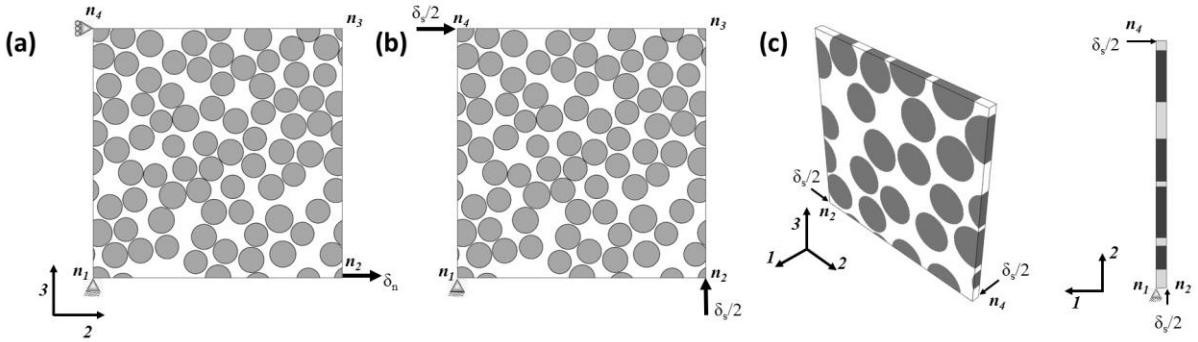

Figure 6: (a) Two-dimensional plane strain analysis of transverse tensile loading, (b) Two-dimensional plane strain analysis of transverse shear loading, (c) Three-dimensional analysis of in-plane shear loading

Periodic Boundary Conditions and Mechanical Loading

The micromechanical analyses used periodic boundary conditions (PBCs) to ensure a macroscopically homogeneous stress/displacement field exists across the boundaries of the RVE (Van der Sluis *et al.* 2000, Tereda *et al* 2000). PBCs consist of a series of kinematic boundary ties to ensure that, in deformed configurations, there is both stress and displacement continuity on opposing RVE boundaries, which maintains spatial periodicity and allows the micro to macro transition. In three-dimensions, the periodic boundary conditions may be expressed as,

$$\begin{aligned} \mathbf{u}(0, x_2, x_3) - \mathbf{u}(t, x_2, x_3) &= \mathbf{u}_1 \\ \mathbf{u}(x_1, 0, x_3) - \mathbf{u}(x_1, l, x_3) &= \mathbf{u}_2 \\ \mathbf{u}(x_1, x_2, 0) - \mathbf{u}(x_1, x_2, h) &= \mathbf{u}_3 \end{aligned} \qquad \textbf{(3)}$$

where $\mathbf{u}_1$, $\mathbf{u}_2$ and $\mathbf{u}_3$ are the displacement vectors which relate the displacements on opposite faces of the RVE shown in Figure 6(c), while *t*, *l*, and *h* correspond to the RVE dimensions in the *1*-, *2*- and *3*-directions, respectively. These conditions are used to impose a range of deformation modes on RVE models to characterise material behaviour.

The micromechanical analysis considers both two- and three-dimensional models. In the case of two-dimensional plane strain models, it is assumed that loading occurs in the *2-3* plane and kinematic ties are therefore only active in the *2*- and *3*-directions. For transverse tensile loading, a relative displacement is applied in the *2*-direction (δ_t) through the control node n_2, such that $\mathbf{u}_2 = (0, \delta_t, 0)$, as shown in Figure 6(a). In a similar fashion, transverse shear loading may be induced by applying a relative displacement in the *2*- and *3*-directions (δ_s) through the control nodes n_2 and n_4, such that $\mathbf{u}_2 = (0,0,\delta_s/2)$ and $\mathbf{u}_3 = (0,\delta_s/2,0)$, as shown in Figure 6(b). Similarly, in three-dimensions (see Figure 6(c)), in-plane shear may be applied using a relative displacement in the *1*- and *2*-directions through the control nodes n_2 and n_4, such that $\mathbf{u}_1 = (0,\delta_s/2,0)$ and $\mathbf{u}_2 = (\delta_s/2,0,0)$, as shown in Figure 6(c). The control node, n_1, remains fully constrained throughout to prevent rigid body motion during deformation. Note that throughout this chapter, these loading regimes, which do not include thermal residual stresses, are referred to as the Mechanical Loading (ML) cases.

Thermal Loading

The effect of thermal residual stresses has also been considered in a number of the micromechanical models presented. These are formed during cooling of the material from cure temperature (448K) to room temperature (298K). To characterise the effect of thermal residual stress on the macroscopic behaviour of the material, an initial thermal load, ΔT = -150 K, was applied globally to each node in the RVE and this was subsequently followed by a mechanical load, as described above. Note that throughout this chapter, this loading regime is referred to as the Thermo-Mechanical Loading (TML) case.

Volume-Based Homogenisation

The homogenisation procedure relates the microscopic state variables, in this case the local stress and strain fields, to the macroscopic averaged quantities. In order to evaluate the average stresses ($\bar{\sigma}_{ij}$) and strains ($\bar{\varepsilon}_{ij}$) over the RVE, the following relations may be used,

$$\bar{\sigma}_{ij} = \frac{1}{V}\sum_{k=1}^{n}\left(\sigma_{ij\,k} V_k\right) \tag{4}$$

$$\bar{\varepsilon}_{ij} = \frac{1}{V}\sum_{k=1}^{n}\left(\varepsilon_{ij\,k} V_k\right) \tag{5}$$

where V is the total volume of the RVE, k is the element number, V_k is the volume of element k in the finite element mesh, n is the total number of elements and σ_{ij} and ε_{ij} are the ij stresses and strains, respectively, in the element k. The effective properties can determined from the relevant stress-strain ratio for a given loading condition, i.e.,

$$E_{ij} = \frac{\bar{\sigma}_{ij}}{\bar{\varepsilon}_{ij}} \tag{6}$$

Surface-Based Homogenisation

A surface based homogenisation scheme may be more conveniently used to determine the average stresses ($\bar{\sigma}_{ij}$) and strains ($\bar{\varepsilon}_{ij}$) of an RVE undergoing microscopic damage processes. This involves computing the average stresses from surface tractions acting on edges (2D) or faces (3D) of an RVE.

14.3.2 Constituent Material Behaviours

Fibres

The HTA fibres were assumed here to be orthotropic linear elastic, and their mechanical properties were taken from Fiedler *et al.* (2005a) and are listed in Table 1.

Table 1: Constituents' Thermo-Mechanical Properties (Fiedler et al. 2005a)

Matrix

The 6376 epoxy matrix was assumed to be an elastic-plastic solid whose thermo-elastic constants are summarised in Table 1. The yielding behaviour of the polymer matrix is sensitive to hydrostatic stress, and as a result the Mohr-Coulomb yield criterion was employed. The Mohr-Coulomb criterion states that yielding will occur on a given plane when the shear stress (τ) exceeds the cohesive stress of the material plus the frictional force acting along the failure plane, such that,

$$\tau = c - \sigma_n \tan\phi \tag{7}$$

where c is the cohesion yield stress, σ_n is the normal stress acting on the failure plane and ϕ is the angle of internal friction. In Mohr's stress plane (see Figure 7(a)), the yield surface of the Mohr-Coulomb model can be expressed in terms of the maximum and minimum principal stresses such that,

$$f(\sigma_1,\sigma_3) = (\sigma_1 - \sigma_3) + (\sigma_1 + \sigma_3)\sin\phi - 2c\cos\phi = 0 \tag{8}$$

where σ_1 and σ_3 are the maximum and minimum principal stresses, respectively. For the Mohr-Coulomb model, the cohesion stress and the angle of internal friction can be related to the tensile (σ_T) and compressive (σ_C) strengths of the material by the following expressions,

$$\sigma_T = 2c\frac{\cos\phi}{1+\sin\phi} \tag{9}$$

$$\sigma_C = 2c\frac{\cos\phi}{1-\sin\phi} \tag{10}$$

Based on the tensile and compressive strengths of the 6376 matrix (σ_T = 103 MPa and σ_C = 264 MPa) Fiedler *et al.* (2005b), the internal friction angle and cohesion stress for the 6376 epoxy matrix were found to be ϕ = 26° and c = 82 MPa, respectively. A non-associative flow rule was used to compute the direction of plastic flow in which the dilatant angle is assumed to be zero.

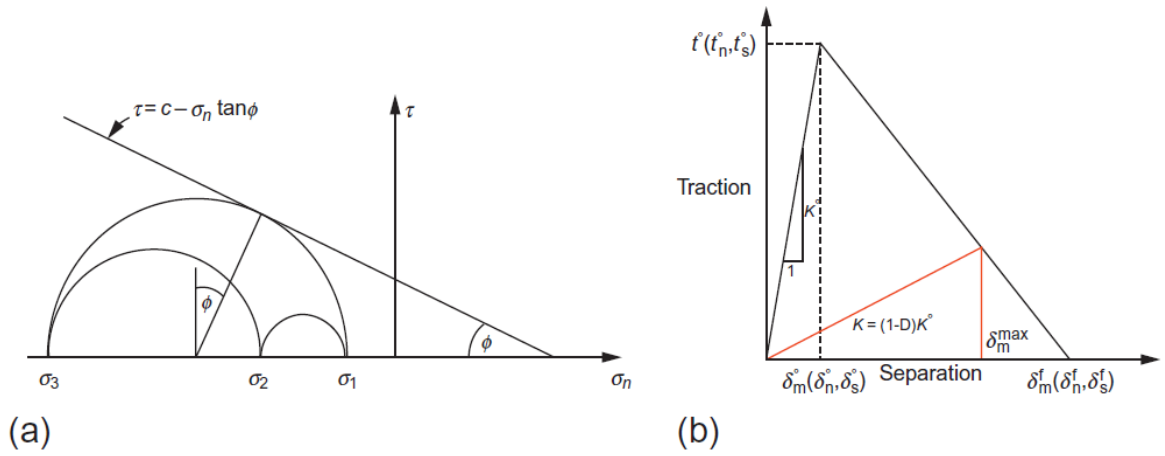

Figure 7: (a) Mohr-Coulomb yield locus in the Mohr stress space. (b) Traction-separation law governing behaviour of cohesive elements

Fibre-matrix interface

The behaviour of the fibre-matrix interface was modelled using cohesive elements available in ABAQUS, which introduce a displacement discontinuity at the fibre-matrix interface when the local stress satisfies a critical condition. Their constitutive response is defined in terms of a traction-separation law which relates the separation displacement between the top and bottom faces of the element to the traction vector acting upon it. Figure 7(b) shows the initial response of the traction separation model is assumed to be linear elastic. An initial elastic stiffness of $K = 10^5$ GPa/m was used to ensure the displacement continuity at the interface in the absence of damage. The initial linear response is followed by the initiation of damage, based on the maximum stress criterion, which is followed by linear softening. Failure of the interface initiates when either the normal stress (t_n) or the shear stress (t_s) exceed the pre-defined normal (t_n^o) or shear (t_s^o) strengths. The evolution of damage at the interface is controlled by a linear softening curve meaning that once the failure stress is exceeded, the element stiffness reduces linearly until complete failure at a specified normal (δ_n^f) or shear (δ_s^f) displacement. This effective displacement at failure (δ^f) determines the rate of damage in the element and this was defined in terms of the fracture energy, Γ, which corresponds to the area under the traction separation curve. For simplicity, it was assumed that the interfacial normal strength was equal to the interfacial shear strength, i.e. $t_n^o = t_s^o$, and the fracture energies were the same for Mode I and Mode II type failure. Different normal and interfacial shear strengths and mode mixity have also been implemented, and the reader is referred to O'Dwyer *et al.* (2014) for more details.

14.4. Prediction of Mechanical Behaviour

14.4.1 Homogenised Effective Properties

Within the linear regime, effective properties were calculated for numerically generated microstructures of increasing size using a volume-averaged homogenisation procedure. Twenty microstructures were generated using the NNA at each value of δ and Figures 8(a) and 8(b) show the mean values of the homogenised effective properties. Error bars have been included indicating the maximum and minimum values calculated at each value of δ, with a large variance evident at low values of δ as a result of the wide range of fibre volume fractions, caused by boundary effects. It was determined that the effective properties converged to a constant value when δ=20, where it was found that the maximum and minimum values of all 20 generated microstructures fell within 10% of the mean values and showed good correlation to experimental results.

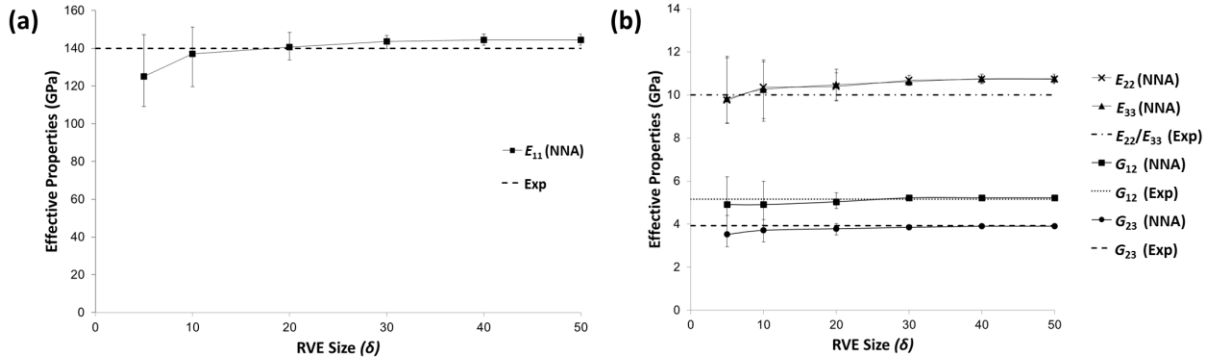

Figure 8: Effective properties of the numerically generated microstructures in (a) the longitudinal direction and (b) the transverse and in-plane directions (Experimental values (denoted by 'Exp') are taken from O'Higgins et al. (2008).)

14.4.2 Interfacial stress state under transverse loading

Radial plots of the stress distribution within the interface, following the approach outlined in Hojo *et al.* (2009) are shown in Figures 9 and 10. The plots have been arranged such that the highlighted fibre in Figure 10(a) has been isolated and compared to the single fibre case in Figure 9(a). The normal (t_n) and shear (t_s) tractions in the interface of the fibre have been plotted radially. The edge of the fibre represents the zero axis for t_n and t_s. The absolute value of t_s has been plotted for clarity (as positive and negative shear generally contribute equally to the damage initiation criteria). In addition, negative values of t_n (although shown) are generally not considered in the failure initiation criteria.

Single fibre RVE

A number of important interfacial stress distribution characteristics are visible in Figure 9 for the single fibre case. The most important, with relation to this study, is the relative magnitude of t_n and t_s, shown in Figure 9(b) and 9(c), respectively. Under transverse tension, t_n is twice the magnitude of t_s and no compressive interfacial stress was observed. An analytical solution for this case has been presented previously (Lesne *et al.* 1995) which produces distributions of t_n and t_s, which are almost indistinguishable from those shown here. Under transverse shear, the magnitude of t_n and t_s are equal, with a large compressive t_n stress.

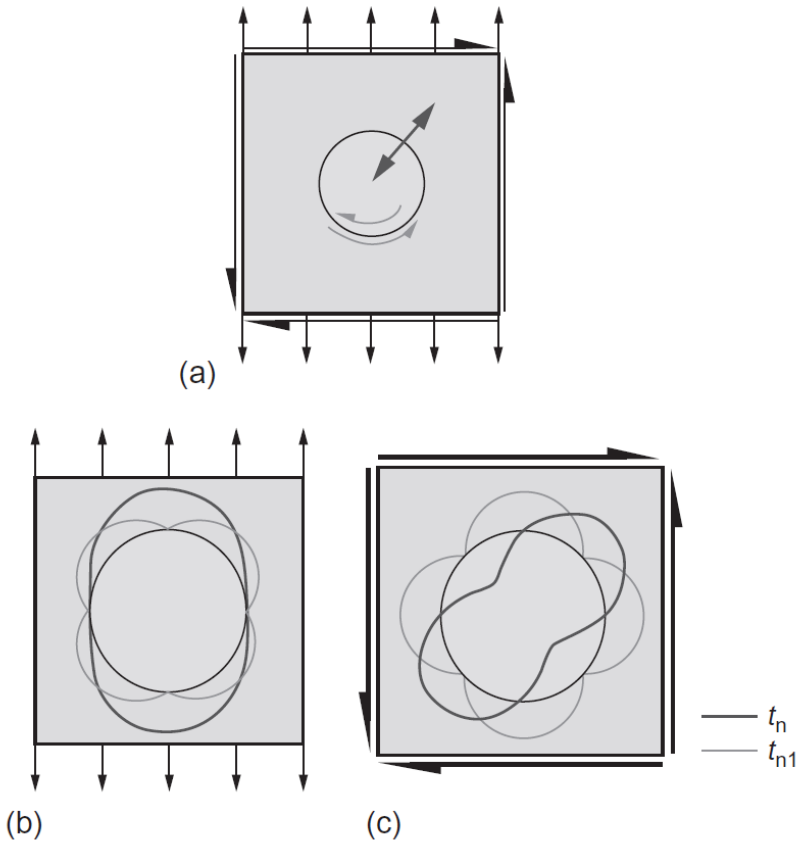

Figure 9: (a) Single fibre RVE; normal and shear interfacial tractions under (b) transverse tension and (c) transverse shear

Multi-fibre RVE

Figure 10(b) and 10(c) show distributions of t_n and t_s for the fibre in Figure 10(a) marked "*A*", in a multi-fibre RVE, generated using the NNA. Under transverse tension and shear, the effect of the neighbouring fibres on the distribution of t_n around the fibre is illustrated by the irregular shape of t_n .Local maxima of t_n are found to be located along lines connecting the centres of the nearest adjacent fibres, and an amplification of t_n relative to t_s was found in comparison to the single fibre case (shown in Figure 9(b)). It can be seen that the shape of the distribution of t_s is not as strongly influenced by the presence of the neighbouring fibres. It can also be seen that t_n is now larger than t_s in both transverse tension and shear, where the magnitude of both were equal in the single fibre case under transverse shear.

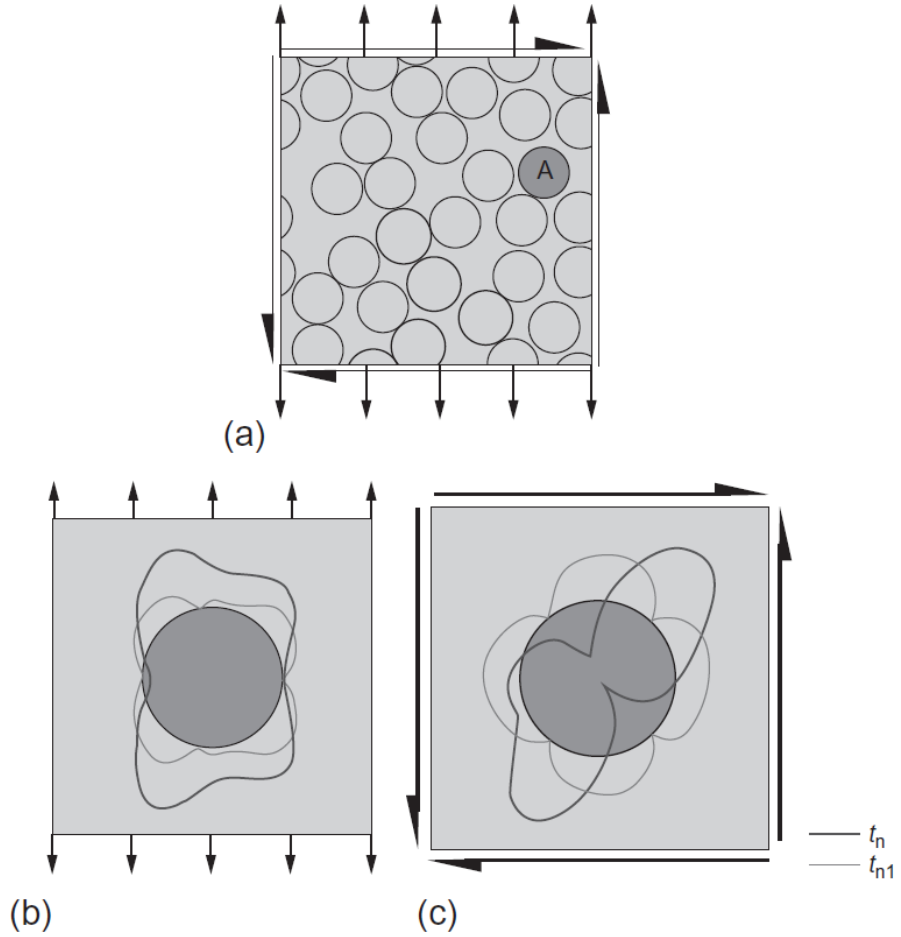

Figure 10: (a) Multi-fibre RVE; normal and shear interfacial tractions under (b) transverse tension and (c) under transverse shear

14.4.3 Micromechanical Damage Models

Effect of fibre–matrix interface strength

Shown in Figure 11(a) is the transverse tensile behaviour of an RVE having a range of interfacial strengths under both Mechanical (ML) and Thermo-Mechanical Loading (TML). The strength of the fibre-matrix interface largely dictated the macroscopic response of the RVE, with a higher transverse strength being seen for increasing fibre-matrix interfacial strength for the ML and TML cases. Under transverse tensile loading, a weak interface ($t^o_{n/s}$ = 15 MPa), results in the lowest transverse strength, with non-linear behaviour observed at a relatively low strain level. Due to the relatively low interfacial strength (compared to the yield stress of the matrix), failure was dominated by fibre-matrix debonding and very little matrix yielding was evident, as shown in Figure 11(b). For a stronger fibre-matrix interface ($t^o_{n/s} = 60$ MPa), matrix yielding becomes more prevalent as the interface strength begins to approach the cohesion stress of the matrix (c = 82MPa) and this interaction between both damage modes was effective in changing the final fracture path of the RVE, as shown in Figure 11(c), when compared to an interface strength of $t^o_{n/s} = 15$ MPa (see Figure 11(b)).

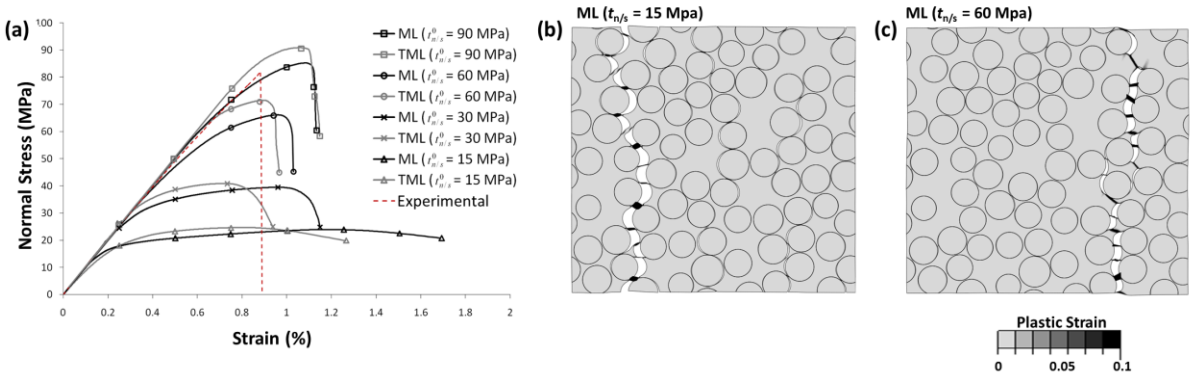

Figure 11 :(a) Transverse tensile behaviour of an RVE generated by the NNA for a range of various interfacial strengths under both mechanical (ML) and thermo-mechanical (TML) loading, compared to experimental results obtained from O'Higgins et al. (2011); Damage progression during transverse tensile loading through an RVE that had a fibre-matrix interface strength of (b) $t_{n/s}$ = 15MPa and (c) $t_{n/s}$ = 60MPa

Shown in Figure 12(a) is the transverse shear behaviour of an RVE having a range of interfacial strengths under both Mechanical (ML) and Thermo-Mechanical Loading (TML). Again, the fibre-matrix interface strength governs the macroscopic response and ultimate strength of the material. For an interfacial strength of $t^o_{n/s} = 60$ MPa, the transverse shear strength is lowest and non-linear behaviour occurs very early in the loading history. Final fracture of the material is manifested as a dominant band of interface cracks orientated approximately perpendicular to the main principal tensile loading axis, as shown in Figure 12(b). For an interfacial strength of $t^o_{n/s} = 120$ MPa, failure of the material is governed by the matrix behaviour as the interface strength is larger than the matrix yield stress (i.e. c = 82 MPa) and the final fracture path is made up of a combination of heavily yielded matrix regions, oriented almost parallel to both the horizontal and vertical shear loading axes, together with a number of interfacial cracks brought about by high shear stresses that resulted from extensive matrix yielding, as shown in Figure 12(c).

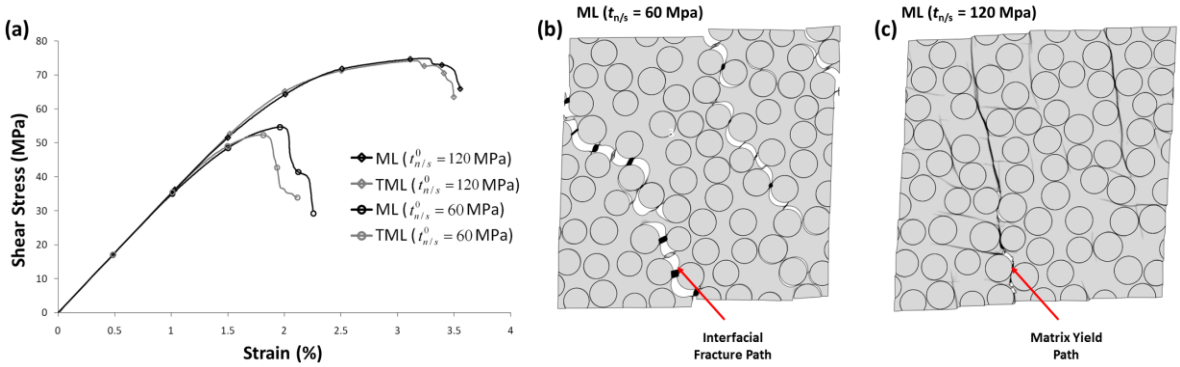

Figure 12: (a) Transverse shear behaviour of an RVE generated by the NNA for a range of various interfacial strengths under both mechanical (ML) and thermo-mechanical (TML) loading; (b) fracture path of the RVE under ML for (b) $t^o_{n/s} = 60$ MPa and (c) $t^o_{n/s} = 120$ MPa

Effect of interface fracture energy

Figure 13(a) shows the transverse shear response of an RVE that had an interfacial strength of $t^o_{n/s} = 60$ MPa for the range of interfacial fracture energies. Increasing the interfacial fracture energy improved both the transverse shear strength and strain-to-failure of the material. It is interesting to compare fracture paths through an RVE for the lowest (Γ=2.5 J/m^2) and highest (Γ=100 J/m^2) fracture energies considered, as shown in Figures 13(b) and 13(c), respectively. For the lowest interface fracture energy (Γ=2.5 J/m^2), damage was limited to the fibre-matrix interfaces and yielding of intermediate matrix bridges between neighbouring debonding fibres. Meanwhile, for the highest fracture energy considered (Γ=100 J/m^2), fibre-matrix debonding was widespread across the RVE and the slow rate of softening at the interface promoted extensive yielding in matrix regions adjoining interfacial cracks, as shown in Figure 13(c). The slow rate of softening leads to a higher transverse shear strength, and means that damage is more effectively dissipated over the entire RVE, producing favourable response characteristics, such as increased strength and higher strain to failure.

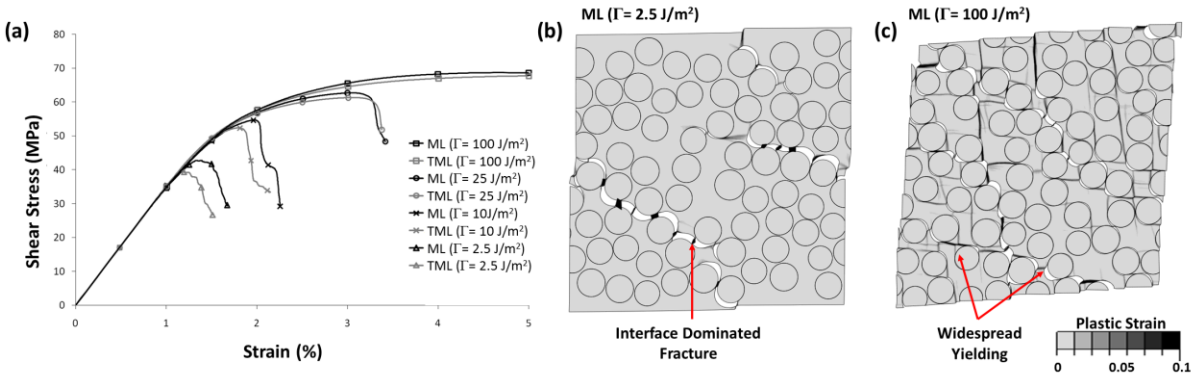

Figure 13: (a) Effect of fracture energy on transverse shear behaviour; Progression of damage through an RVE with interfacial fracture energies of (b) Γ=2.5 J/m^2 and (c) Γ=100 J/m^2

14.4.4 Damage accumulation under cyclic loading

Composite materials exhibit a sequential accumulation of a multitude of hierarchical dissipative mechanisms, whose initiation and subsequent propagation depends heavily upon the loading history. Micromechanics may be used to illustrated this complex damage accumulation process by subjecting an RVE ($t^o_{n/s} = 90$MPa, Γ=10 J/m^2) to a regime of successive transverse tensile (ε_{22} = 1%) and compressive (ε_{22} = -2%) loadings, followed by a subsequent transverse tensile load to failure ($\varepsilon_{22} = \varepsilon_f$). Figure 14 shows that the initial transverse tensile load (Path O-A) causes non-linear behaviour as a result of fibre-matrix debonding and yielding in the matrix, which are shown for the Load Point A in the RVE insert to Figure 14(a). The unloading path of the material (Path A-B) shows a reduced slope denoting a loss in material stiffness caused by crack opening at fibre-matrix interfaces. Also, unloading does not take place through the origin (O) as some permanent plastic strain remains in the material. However, crack closure does occur at debonded interfaces during the unloading phase, as shown by the

final configuration of the RVE at the Load Point B in the RVE insert to Figure 14(b). Upon subsequent compressive loading (Path B-C), the compressive modulus is recovered to almost that of the undamaged material as a result of crack closure and compressive load take up between the newly formed crack faces. Further non-linear behaviour in the compressive loading phase is seen as a result of more fibre-matrix debonding and matrix yielding occurring, as shown at the Load Point C in the RVE insert to Figure 14(c). A reduction in the compressive modulus is seen during the next unloading phase (Path C-D) as a result of damage occurring during compressive loading. Again, unloading does not take place through the origin as a new permanent plastic strain exists in the material as a result of the previous loading cycles. Upon subsequent tensile loading (Path D-E), a further reduction in the tensile modulus is also seen (compared to the unloading phase in Path A-B) as a result of cracks developed during the previous compressive loading phase. It is also noticeable that the tensile strength for this cycle has reduced, which indicates that the material was at the cusp of its ultimate tensile strength at Load Point A. The compression damage sustained during the previous load cycle was enough to actually trigger ultimate failure (i.e. Load Point E) in the composite at a lower stress than at Load Point A.

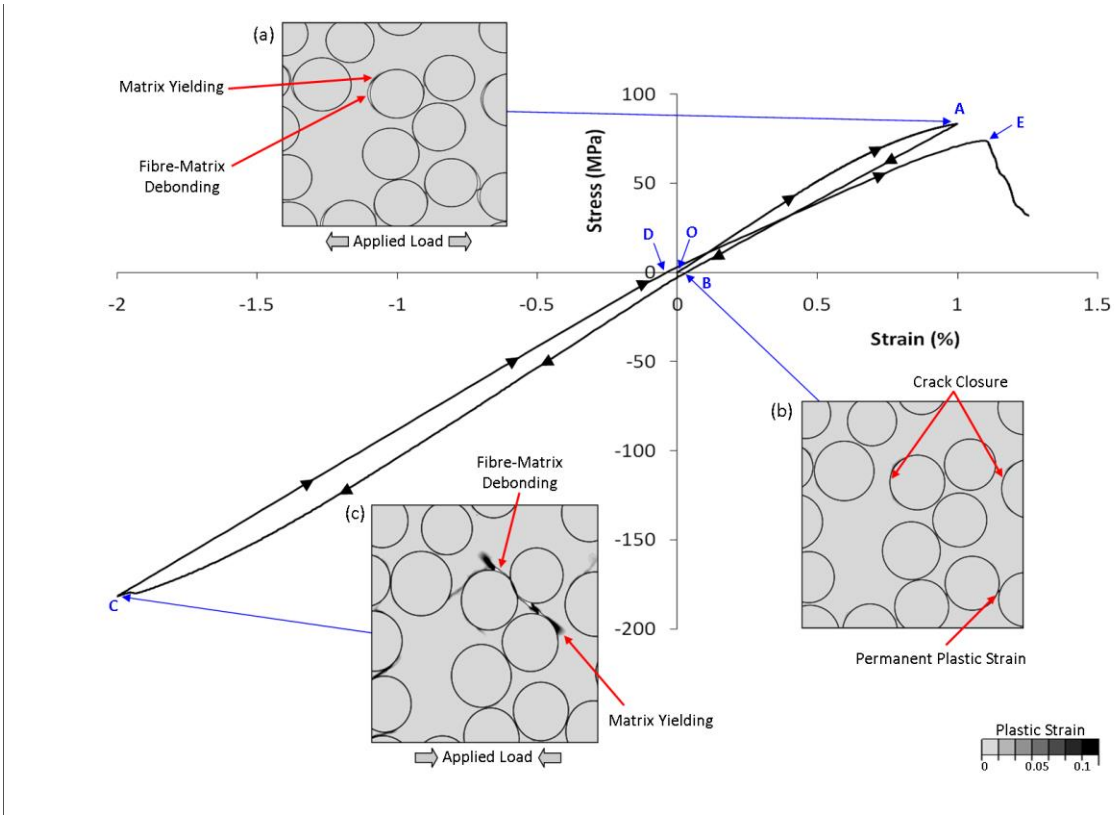

Figure 14: The response of an RVE subject to successive tensile and compressive loading and microscopic damage accumulation observed, (a) following initial tensile loading (Load Point A); (b) following unloading from tensile stress state (Load Point B) and; (c) following subsequent compressive loading (Load Point C) (Note: a deformation scale factor of 5 has been used in the above images)

14.5. Applications to Failure Surfaces and Structural Load Cases

In this section we develop further the micromechanical model to reproduce the well know interactive failure criteria of Hashin (1980). In addition, the model is further extended to a

structural load case where an adhesive bond-line is added to the RVE to form a micromechanical model of a bonded composite joint.

14.5.1 Generation of failure surfaces

Effect of thermal residual stress on transverse failure surface

Failure of the material was predicted under a combination of transverse shear and transverse normal loads to examine the effect of thermal residual stress on the failure surface in the transverse plane. By varying the ratio of the applied transverse shear/normal displacements (δ_s / δ_n), a failure envelope for the material was constructed for both the ML and TML cases. Figure 15 shows the failure envelope generated for both the ML and TML cases in the $\sigma_{22} - \tau_{23}$ .stress space, where an interface strength of $t^o_{n/s} = 60$ MPa and a fracture energy of Γ=10 J/m^2 was assumed, meaning that failure was dominated by interface cracking. The inclusion of thermal residual stress has meant the TML case has been shifted and slightly contracted compared to the ML case. This shift in the fracture surface occurs as, for tension dominated loading, thermal residual stress has a beneficial effect on the failure strength. This is due to the large compressive stresses which exist at the interface following thermal cool-down from cure temperature, which effectively delay the onset of debonding. As the loading begins to become shear dominated, the presence of thermal residual stress begins to affect the fracture surface negatively, as increased interfacial shear stress following the thermal loading phase contributes to earlier failure of the material. For compression dominated loading, thermal residual stress shows slightly negative effects as failure at the interface must occur due to shear failure (note: a compressive stress at the interface cannot cause debonding to occur). The largest difference between the ML and TML failure surfaces occurs for a loading ratio of, $\delta_s / \delta_n = -4$. Interestingly, the fracture path for this loading ratio comprises of a series of interfacial cracks orientated parallel to the horizontal shear loading axis, as shown in Figure 15(c), indicating failure at these interfaces was shear dominated.

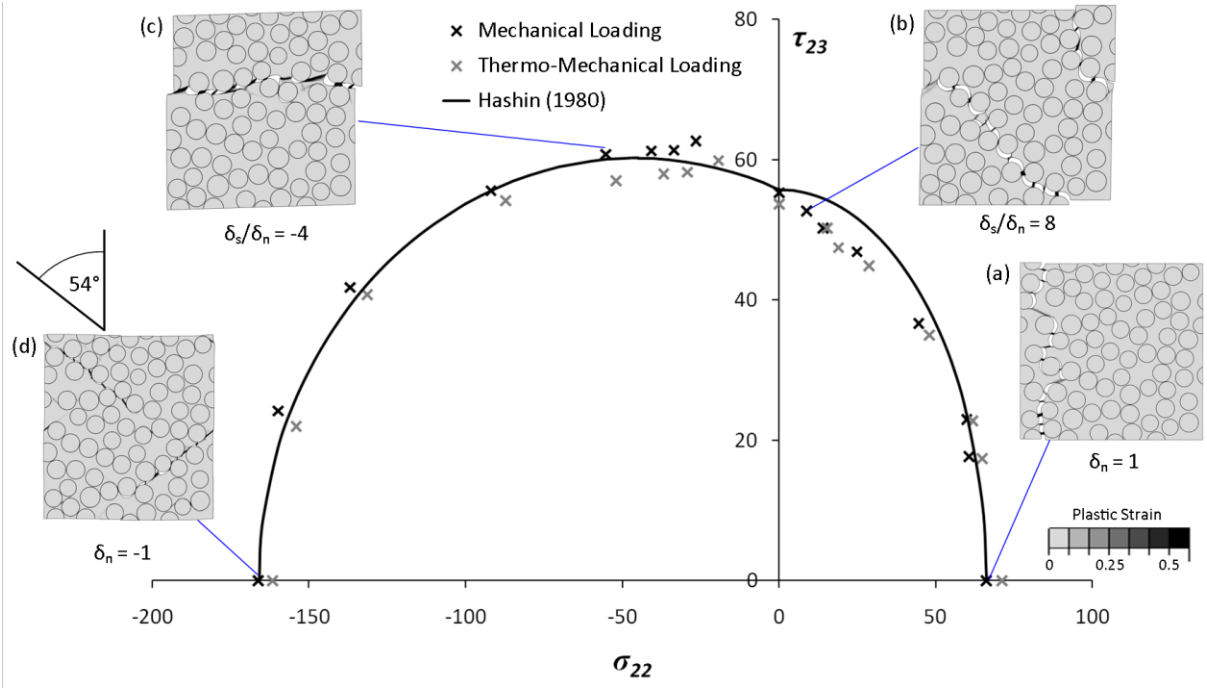

Figure 15: Failure surface generated by micromechanical models using combined transverse normal and shear loading regime

Effect of local fibre volume fraction on transverse failure surface

To consider the effect of fibre volume fraction (V_f) on the transverse behaviour, a series of RVEs were generated with fibre volume fractions of V_f = 20%, V_f = 40% and V_f = 59%. The NNA was used to generate the microstructures for V_f = 59%, while a Hard-Core Model (HCM) was used to generate microstructures for both V_f = 20% and V_f = 40%, as shown in Figure 16(a)-(c). Figure 16(d) shows the effect of fibre volume fraction on the transverse failure surface when a fibre-matrix interface strength of $t^o_{n/s}$ = 60 MPa and a fracture energy of Γ=10 J/m^2 were assumed. For this interface dominated failure, it was found that reducing the fibre volume fraction actually results in a slight expansion of the transverse failure surface. Figure 16(d) shows only a slight difference between the failure surfaces of 40% and 59% fibre volume fraction, however, the 20% fibre volume fraction shows much higher failure strengths for all loading ratios. This higher transverse strength for lower fibre volume fractions can be attributed to the larger inter-fibre spacing between neighbouring fibres (however, it should be noted that the longitudinal strength would decrease with decreasing fibre volume fraction). Thus, in lower fibre volume fraction arrangements, the larger inter-fibre spacing effectively delays the onset of debonding, resulting in higher strengths for each loading ratio. Figure 16(e) shows the effect of fibre volume fraction on the transverse failure surface for a perfect fibre-matrix interface, such that failure was matrix dominated. In contrast to interface dominated failure, reducing the fibre volume fraction in the case of matrix dominated failure resulted in a contraction of the transverse failure surface, as shown in Figure 16(e). This is caused by the lack of reinforcement in low fibre volume fraction configurations, which allows matrix yield paths to propagate more easily.

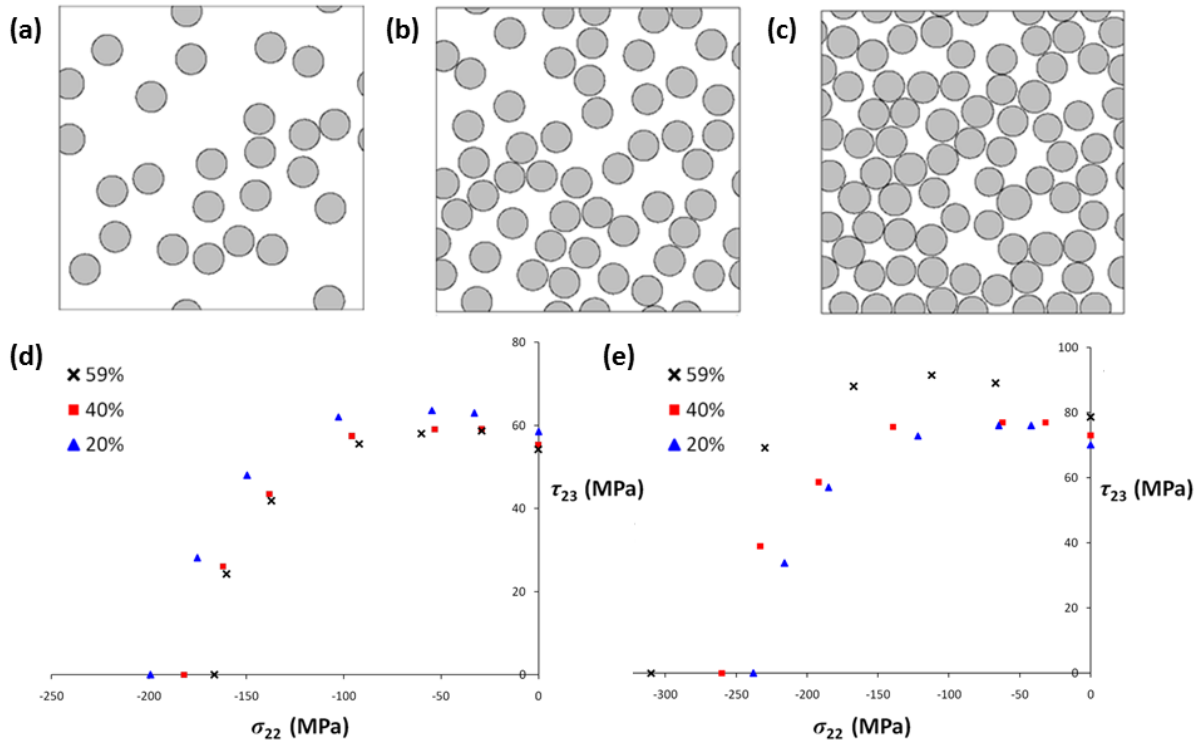

Figure 16: Fibre distributions generated at (a) V_f = 20% (b) V_f = 40% and (c) V_f = 59%; Effect of fibre volume fraction on transverse failure surface for (d) interface dominated failure and (e) matrix dominated failure

14.5.2 Micro-mechanical modelling of bonded composite joints

A novel application of RVE's is to extend and augment them in order to model sub-sections of composite structures. In this case we extend the RVE developed earlier in this chapter to model composite bonded joints. The proposed FE model consists of a microscale RVE of the interface between a composite ply and an adhesive layer, away from the edges of an adhesive joint. The two sections are separated by a damageable interface referred to here as the bond-line. The model is shown in terms of an adhesive single-lap joint with composite adherands in Figure 17, where the axial load, *F*, on the joint induces Mode *I* and Mode *II* deformations on the composite-adhesive interface. The material models used here are similar to those showin in Figure 7, more details are listed inO'Dwyer *et al.* (2013).

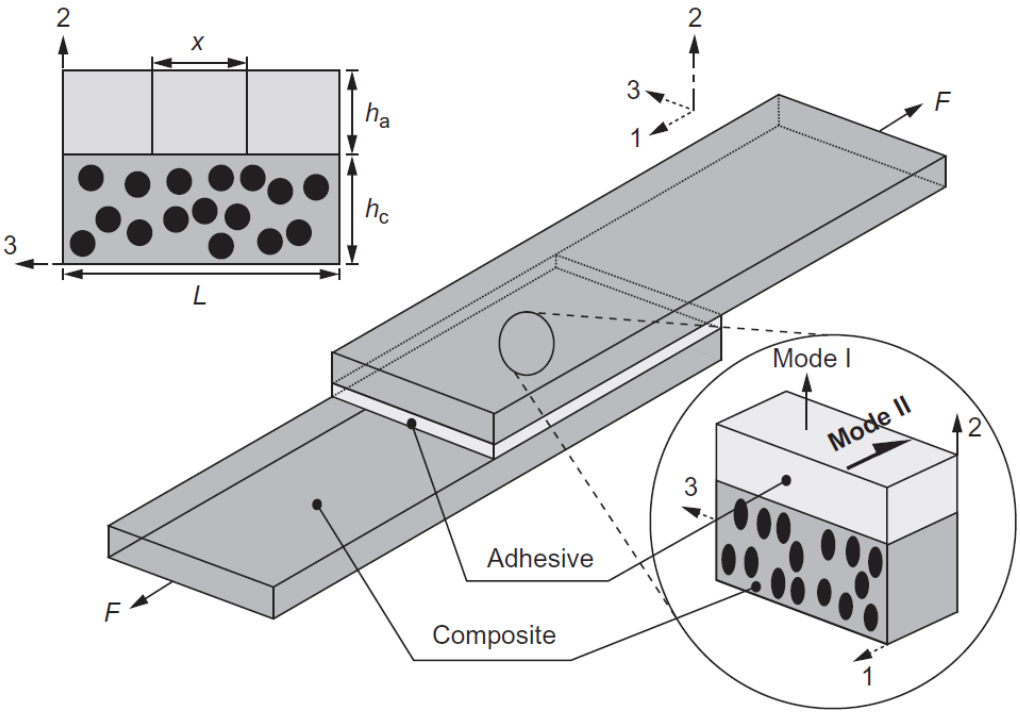

Figure 17: Adhesive layer model as applied to a composite bonded joint, including local reinforcement orientations. The dimensions L *and* x *are the width of the RVE and the weakened central region of the bond-line, respectively*

Bond-line strength effects

A key advantage of modelling sub-sections of bonded joints with micromechanical models is that design variables, such as bond-line strength, can be varied to examine "*what if*" scenarios. In Figure 18(a), the strength of the composite joint is plotted against the bond-line strength (i.e. the composite-adhesive interface strength). It can be seen in Figure 18(a), that under Mode *I* loading, joint strength increases linearly with respect to bond-line strength until a maximum is reached at a bond-line strength (t_n^c) of approximately 77 MPa. Any further increase in bond-line strength produces no increase in joint model strength. This corresponds to the condition where the damage processes transfers from the bond-line to the composite region, as the bond-line strength exceeds that of the composite. Similar trends are found in Figure 18(b), where a plateau is reached once the shear strength of the bond-line (t_s^c) exceeds 25 MPa. This corresponds to the point where the damage process transfers to the adhesive. The critical bond-line strength is slightly lower than the yield point, under shear, of the adhesive, which can be attributed to stress concentrations(caused by the fibres) propagating into the adhesive and initiating adhesive yielding.

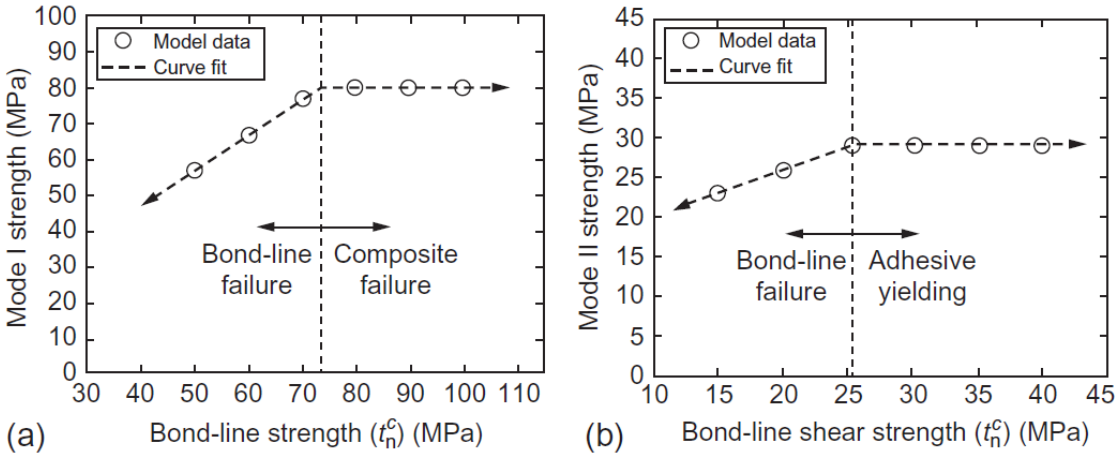

Figure 18: Bond strength variation, (a) Bond-line model strength variation under Mode I*, (b) Bond shear strength variation under Mode II*

Failure modes and modelling first ply failure

Failure at the bond-line and within the composite region has been reported from adhesive bonding tests and a mix of the two failure modes on a single failure surface is also a common result (e.g. Feih & Shercliff 2005; Kim *et al.* 2006). It has been shown that under Mode *I* conditions, the current models are capable of producing failure in the composite and the bond-line separately, depending on the bond-line strength. Hence, in this section a variation in bond-line strength is considered where a central section of the bond-line is weakened. The strong region is assigned a strength of t_n^c = 78 MPa (i.e. just exceeding the strength at which failure was entirely within the composite, see Figure 18(a)). A parameter *W* is introduced as the strength of the weakened region, normalised by the strength of the strong region. The length of the weakened region is varied with relation to the overall bond-line RVE length, *L* (*x* and *L* are shown in Figure 17). Another parameter *w* is introduced to characterise the length of the weakened region as $w = x/L$. Six different lengths of weakened regions were investigated, corresponding to w = 0, 0.2, 0.4, 0.6, 0.8, 1. Three RVEs were analysed at each value of *w* to investigate if fibre distribution influenced the tendency for mixed failure to occur.

Investigations carried out corresponding to W = 0.8, 0.9 resulted in failure of the bond-line, as failure initiated and propagated in the bond-line without debonding occurring in the composite. A central region weakened to W = 0.95 (t_n^c = 74 MPa) produced mixed failure in some cases, the failure pattern being shown in Figure 19. It can be seen that the debonded fibres are predominantly located beneath the section of bond-line which remained intact. The fibres which debonded form the weak point in the loading path in this region, as the bond-line directly above remained intact. In the central region of the RVE, damage initiated at the weakened region of bond-line, preventing debonding of the adjacent fibres. This was common across all mixed failure models, however, some slight overlapping of debonding and bond-line damage was found to occur.

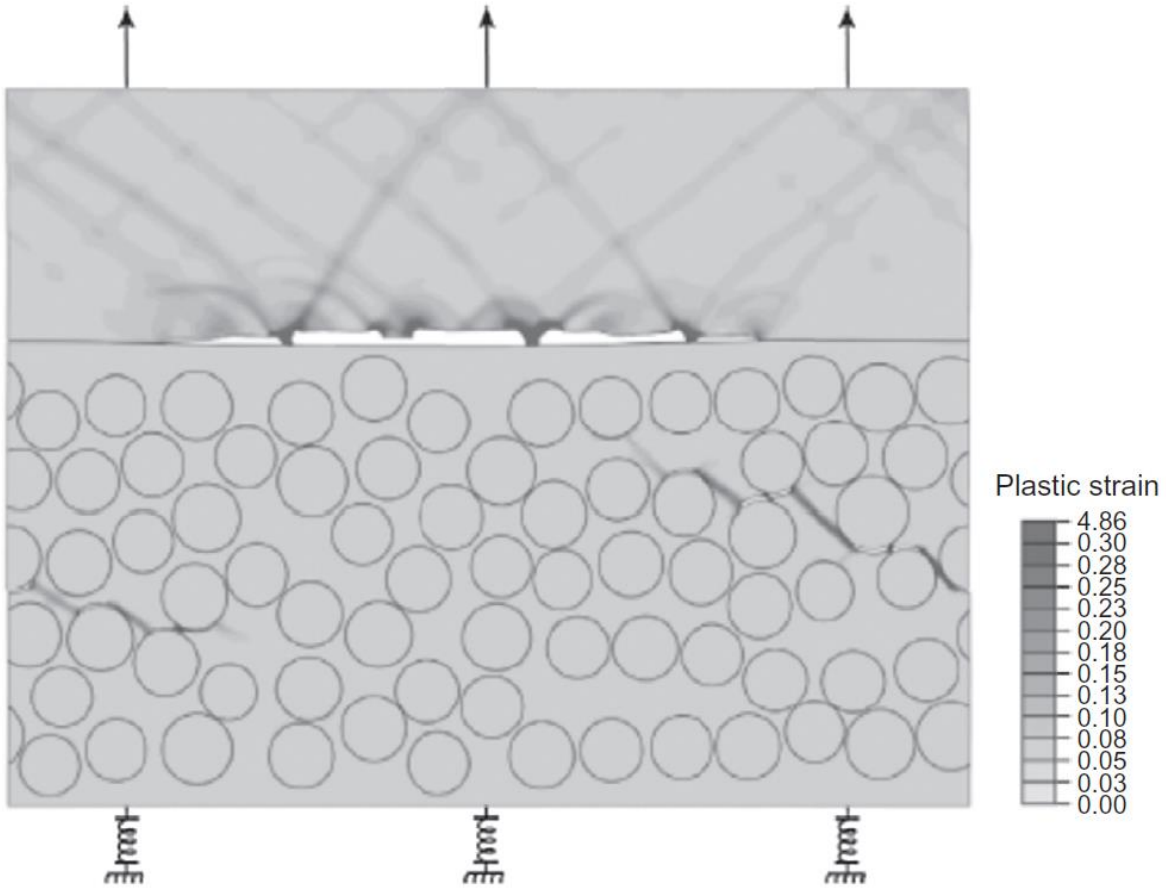

Figure 19: Mixed failure under Mode I loading

14.6 Micromechanical Experimental Calibration and Validation Techniques

This section outlines some very useful and novel experimental techniques that can be used to both calibrate and validate micromechanical finite element models at and/or below the microscale. The list of techniques and equipment is not exhaustive, but does give some insight to what is currently being used by many research institutions concerned with micromechanical characterisation of composites.

14.6.1 In-Situ SEM Micro-testing

Micro testing miniature composite specimens, and indeed composite bonded joints, in the chamber of a Scanning Electron Microscope (SEM) is a relatively new technique, and can be used to understand the failure mechanisms in composites in real-time at, and below, the microscale. Figure 20(a) shows a picture of the micro-test system based at the University of Limerick in a tensile/compression testing configuration, where a miniature single-lap bonded composite joint is in-situ prior to testing. Figure 20(b) shows an image of the micro-scale fracture in this joint during testing. Figure 20(c) demonstrates the resolution that can be achieved, in real time, with this technique, where cracks down to the fibre level scale can be resolved, with clarity, and with local macroscopic load-displacement information superimposed.

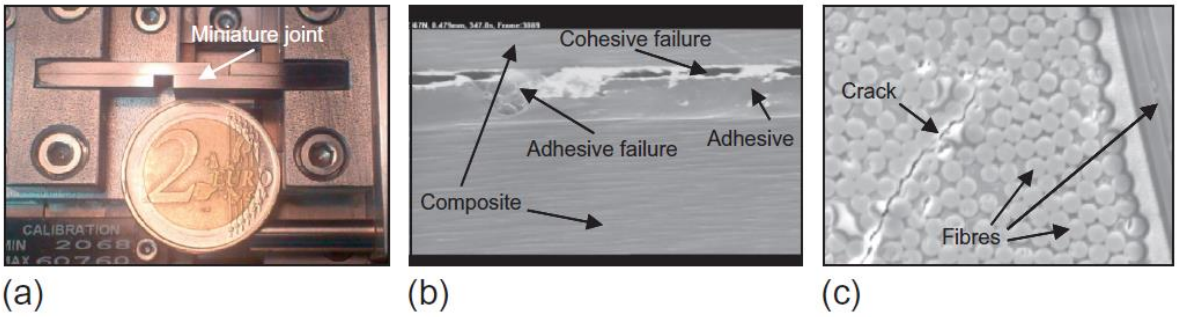

Figure 20: Micro-scale testing of a miniature bonded joint, (a) joint in-situ before testing, (b) cohesive and adhesive failure, (c) fibre level scale crack growth observable

14.6.2 Nano-indentation to determine fibre, matrix and fibre-matrix interphase properties

Nano-indentation using a continuous stiffness mode, which can determine the hardness and modulus of a surface as a function of depth into the surface, is a very useful technique to locally determine the mechanical properties of the fibres, matrix and fibre-matrix interphase (Hodzic 2001a) at and below the microscale for input into micromechanical models, where material property homogeneity cannot be assumed. Figure 21(a) shows a nano-indent into a resin rich pocket of a unidirectional composite carried out recently by the authors. In addition, nano-scratch is another useful technique to determine the change in material properties across a surface, and a combination of both techniques can yield a surface field measure of mechanical properties (Hodzic 2001b). State-of-the-art nano-indentation facilities can also scan the surface of the indentation or scratch using the indenter tip (just like an Atomic Force Microscope) to yield important pile-up information around the indenter tip, which can be used to determine other physical properties of composites, such as plasticity in the matrix. Figure 21(b) shows one such scan on a composite carried out for a pending publication by the authors, where it can be clearly seen that significant pile-up occurred around the matrix.

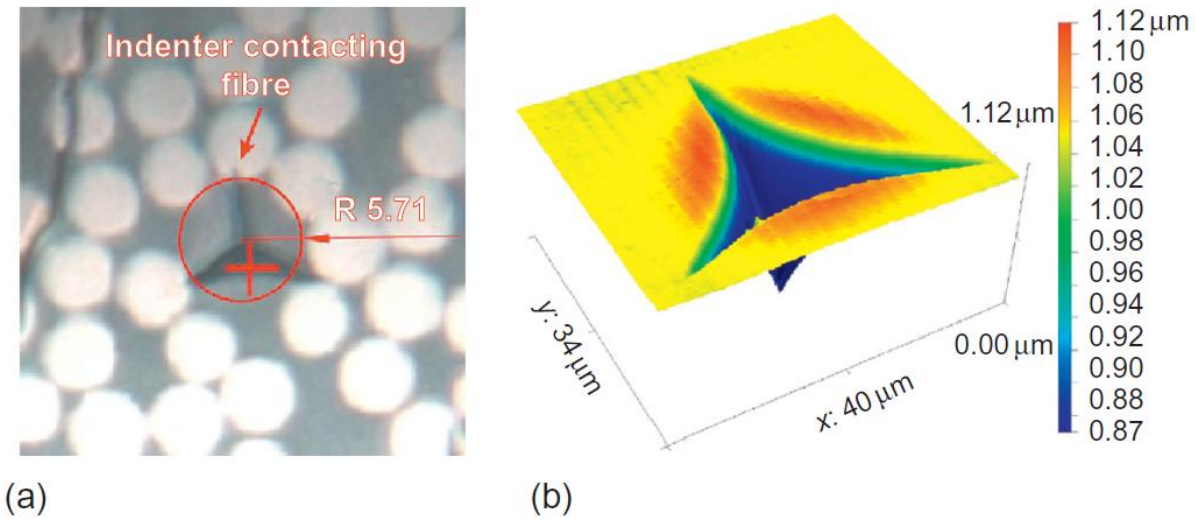

Figure 21: (a) Nano-indentation into a resin pocket in a carbon fibre composite, (b) a nano-scan showing matrix pile-up around the residual indentation impression

14.6.3 3D Micro-CT for NDI evaluation

Three-dimensional Micro-CT is a very powerful non-destructive technique to examine the surface and sub-surface material composition and integrity of composites. Figure 22 shows a scan of a carbon-fibre-PEEK epoxy composite, where it can be clearly seen that relatively large volumes of composite can be scanned in three-dimensions down to the fibre level scale. Also, what makes this approach particularly attractive is the ability to isolate fibres from the matrix, as shown in Figure 22(a), and the ability to isolate and examine voids in the matrix, as shown in Figure 22(b). For fibre level detail scanning, ultrahigh resolution detectors are normally required and sample volumes tend to be very small ($\approx 1 mm^3$).

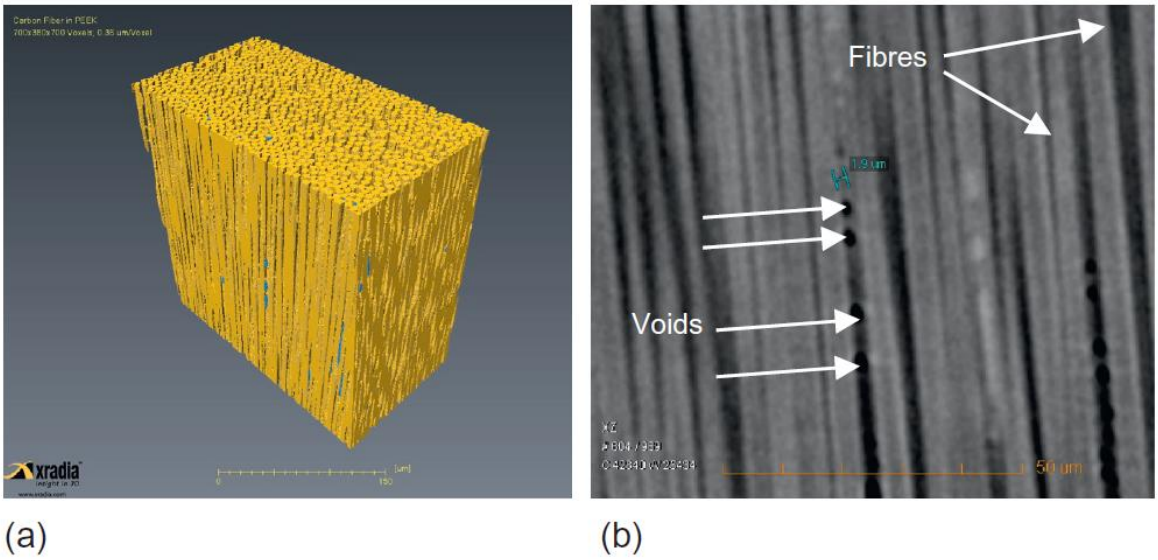

Figure 22: Micro-CT images of a carbon-fibre composite sample, (a) carbon fibres isolated from the matrix, (b) cross-section showing the voids in the composite

14.7. Conclusions and Ways forward

14.7.1 Conclusions of the chapter

This chapter has set out to introduce the reader to the important area of micromechanical modelling for the analysis of failure in advanced composite materials. The previous sections have demonstrated the details of how such models are formed and then used to solve complex problems in composites at both material and structural levels. While the micromechanical models require a solid understanding of composites, geometric topology, finite element analysis and non-linear material modelling, once they are created they can be used for extensive and cost efficient parameter studies for both materials and structural design. Automated tools which shield the user from this extensive *know-how* are now available on the market (e.g. see McCarthy & Vaughan 2012). Experimental techniques described herein are used to both calibrate and validate the micro-mechanical models. However, at and below the micro-scale great care is needed to interoperate results from these experiments, and to extract useful material property information for input to the micromechanical models.

14.7.2 Future Research Topics

The most immediate area for further research is the development of a damage model for the epoxy matrix (and the adhesive materials for joint micromechanical models). Micro-cracking of both the matrix (and the adhesive materials) can increase the energy absorbing capacity during crack growth in the composite (at the composite-adhesive interface) and the inclusion of such energy absorbing mechanisms would improve the correlation between the modelling

and experiments. Extended finite element approaches, where matrix cracks could be modelled discretely, may be a useful numerical technique to solve this problem.

Delamination of composite plies is an underdeveloped area of micromechanical analyses. Such a case was investigated by Ye and Chen (2011) for single fibres at different orientations, however, the case has of randomly distributed fibres has not been investigated. Interactions of the stress fields in plies orientated at different angles opens the possibility for premature yielding of the matrix and interfacial damage to occur. Three dimensional stress gradients would be induced during loading, and RVEs would be required to be sufficiently large to capture the gradients in their entirety. This model would therefore suffer from high computational costs, but would provide new insight into the causes of delamination of composite materials and damage progression during delamination. In addition, the model could be adapted to investigate the stress distributions related to different ply orientations within a laminate and such a study could reveal whether stress distributions between certain ply orientations in a laminate cause more critical stress concentrations, and could aid in optimisation of ply orientations for different boundary value problems.

True multi-scale analysis of composites damage is another area for potential future development. With this approach, micro-mechanical models would be linked to macroscopic models of composite materials and/or structures, and a real time link, with feedback, would be provided between both scales. Hence once damage was predicted to initiate at the macroscale, a micromechanical model of the failing region would be formed (with appropriate boundary conditions). The micromechanical model would then predict the "true" damage response at the microscale and feed the effects of this damage back to the macroscale model, which would then need to be updated. This would be an iterative process as the damage develops, and so would require extensive computational power.

With reference to experiments, DIC techniques, in tandem with in-situ SEM testing provide an opportunity to validate the crack path prediction of micromechanical models. A possible approach is to extract exact fibre positions at the start of an in-situ SEM video, and export these positions to a microscale FEA model. Validation of the crack path prediction of the microscale models could then be achieved through application of appropriate boundary conditions to the model, to correspond to the conditions applied in the test. Direct comparison of the experimental crack path and the path predicted at the microscale could be made, and the method could be used to further refine and tune the parameters of micromechanical models.

14.7.3 Related Journals, Conferences

Many scientific and engineering journals publish papers on micromechanical modelling of composite materials, and the reader is referred to the reference section of this chapter for a comprehensive list of relevant papers.

14.8. Acknowledgments

This publication has emanated from research conducted with the financial support of Science Foundation Ireland under Grant Number SFI 10/RFP/MTR2884. The authors would also like to thank Noel O'Dowd, Donal O'Dwyer, Mark Hardiman, Andrew Keane and Daniel Mortell for their many useful contributions to this work over the past number of years.

14.9. References

Hinton, M. J. and P. D. Soden (1998). 'Predicting failure in composite laminates: the background to the exercise' Composites Science and Technology 58(7): 1001-1010.

O'Dwyer DJ, O'Dowd NP and McCarthy CT (2013), 'Micromechanical investigation of damage processes at composite-adhesive interfaces', Composites Science and Technology, 86: 61-69.

O'Dwyer DJ, O'Dowd NP and McCarthy CT (2014), Numerical micromechanical investigation of interfacial strength parameters in a carbon fibre composite material, Journal of Composite Materials, 48(6): 749-760

O'Dwyer DJ, O'Dowd NP and McCarthy CT (2012). Investigation of strain hardening effects under in-plane shear of unidirectional composite materials. Comp Mater Sci.,64:179-82.

Hardiman M, Vaughan TJ, and McCarthy CT (2012). The effect of fibre constraint in the nanoindentation of fibrous composite microstructures: A finite element investigation. Comp Mater Sci. 2012;64:162-7.

Vaughan TJ and McCarthy CT (2010). A combined experimental-numerical approach for generating statistically equivalent fibre distributions for high strength laminated composite materials. Composites Science and Technology, 70(2):291-7.

Vaughan TJ and McCarthy CT (2011a). Micromechanical modelling of the transverse damage behaviour in fibre reinforced composites. Composites Science and Technology, 71(3):388-96.

Vaughan TJ and McCarthy CT (2011b). A micromechanical study on the effect of intra-ply properties on transverse shear fracture in fibre reinforced composites. Composites Part a-Applied Science and Manufacturing, 42(9):1217-28.

McCarthy CT and Vaughan TJ (2012). COMM Toolbox: A MATLAB toolbox for micromechanical analysis of composite materials. Journal of Composite Materials, 46(14):1715-29.

Vaughan TJ, McCarthy CT and McNamara LM (2012). A three-scale finite element investigation into the effects of tissue mineralisation and lamellar organisation in human cortical and trabecular bone. J Mech Behav Biomed, 12:50-62.

Hobbiebrunken, T., M. Hojo, T. Adachi, C. De Jong and B. Fiedler (2006). 'Evaluation of interfacial strength in CF/epoxies using FEM and in-situ experiments' Composites Part A: Applied Science and Manufacturing, 37(12):2248-2256.

Lafarie-Frenot, M. C., C. Hénaff-Gardin and D. Gamby (2001). 'Matrix cracking induced by cyclic ply stresses in composite laminates' Composites Science and Technology, 61(15): 2327-2336.

O'Higgins, R. M., C. T. McCarthy and M. A. McCarthy (2011). 'Identification of Damage and Plasticity Parameters for Continuum Damage Mechanics Modelling of Carbon and Glass Fibre-Reinforced Composite Materials, 47(1): 105-115.

González, C. and J. Llorca (2007). 'Virtual fracture testing of composites: A computational micromechanics approach' Engineering Fracture Mechanics, 74(7): 1126-1138.

Brockenbrough, J. R., S. Suresh and H. A. Wienecke (1991). 'Deformation of metal-matrix composites with continuous fibers: geometrical effects of fiber distribution and shape' Acta Metallurgica Et Materialia, 39(5): 735-752.

Bohm, H. J. (1998). A short introduction to the basic aspects of continuum micromechanics, Institute of Lightweight Design and Structural Biomechanics (ILSB), Vienna University of Technology.

Trias, D. (2005) 'Analysis and Simulation of Transverse Rando Fracture of Long Fibre Reinforced Composites ' Dep. dEnginyeria Mecanica i de la Construccio Industrial, Girona, University of Girona. Ph.D. Thesis.

Pindera, M.-J., H. Khatam, A. S. Drago and Y. Bansal (2009). 'Micromechanics of spatially uniform heterogeneous media: A critical review and emerging approaches' Composites Part B: Engineering, 40(5):349-378.

Grufman, C. and F. Ellyin (2008). 'Numerical modelling of damage susceptibility of an inhomogeneous representative material volume element of polymer composites' Composites Science and Technology, 68(3-4):650-657.

Ghosh, S., J. Bai and P. Raghavan (2007). 'Concurrent multi-level model for damage evolution in microstructurally debonding composites' Mechanics of Materials 39(3): 241-266.

de Boer, H. and G. Poort (2010). Multiscale damage modelling in Abaqus. IV European Conference on Computational Mechanics. Paris.

Firehole Technologies Inc (2009). Helius:MCT. Laramie, WY.

Diggle, P. (2003). Statistical Analysis of Spatial Point Patterns. London, Arnold.

Ripley, B. D. (1977). 'Modelling Spatial Patterns' Journal of the Royal Statistical Society: Series B (Statistical Methodological), 39(2): 172-212.

Fiedler, B., A. Gagel, T. Hobbiebrunken, K. Schulte, M. Hojo and S. Ochiai (2005a). 'Modelling of the transverse strength of fibre reinforced epoxy composite at low and high temperature' Composite Interfaces 12(3/4): 379-394.

Fiedler, B., T. Hobbiebrunken, M. Hojo and K. Schulte (2005b). Influence of Stress State and Temperatrue on the Strength of Epoxy Resins. 11th International Conference on Fracture (ICF 11),. Turin, Italy, on CD.

O'Higgins, R. M., M. A. McCarthy and C. T. McCarthy (2008). 'Comparison of open hole tension characteristics of high strength glass and carbon fibre-reinforced composite materials' Composites Science and Technology, 68(13): 2770-2778.

Hojo, M., M. Mizuno, T. Hobbiebrunken, T. Adachi, M. Tanaka and S. K. Ha (2009). 'Effect of fiber array irregularities on microscopic interfacial normal stress states of transversely loaded UD-CFRP from viewpoint of failure initiation' Composites Science and Technology, 69(11-12): 1726-1734.

Lesne PM, Allio N and Valle R (1995). 'Combined effects of the fibre distribution and of the fibre matrix or interphase matrix transverse modulus ratio on the possible fracture modes of unidirectional composites submitted to a transverse loading. Acta Metall Mater, 43(12): 4247–4266.

Hashin, Z. (1980). 'Failure criteria for unidirectional composites' Journal of Applied Mechanics, 47: 329-335.

Feih S and Shercliff HR (2005). Adhesive and composite failure prediction of single-L joint structures under tensile loading. Int J Adhes Adhes, 25(1):47–59.

Kim KS, Yoo JS, Yi YM and Kim CG (2006). Failure mode and strength of uni-directional composite single lap bonded joints with different bonding methods. Compos Struct, 72(4):477–85. 70.

Hodzic A, Stachurski ZH and Kim JK, (2001a), Nano-indentation of polymer-glass interfaces Part I. Experimental and mechanical analysis, Polymer, 41(18):6895–6905.

Hodzic A, Kalyanasundaram S, Kim JK, Lowe AE and Stachurski ZH (2001b), Application of nano-indentation, nano-scratch and single fibre tests in investigation of interphases in composite materials, Micron, 32(8):765–775.

Ye, Q. and Chen, P. (2011), 'Prediction of the cohesive strength for numerically simulating composite delamination via CZM-based FEM', Composites Part B: Engineering, 42(5), 1076–1083.

Terada, K., M. Hori, T. Kyoya and N. Kikuchi (2000). 'Simulation of the multi-scale convergence in computational homogenization approaches' International Journal of Solids and Structures 37(16): 2285-2311.

Van der Sluis, O., P. J. G. Schreurs, W. A. M. Brekelmans and H. E. H. Meijer (2000). 'Overall behaviour of heterogeneous elastoviscoplastic materials: effect of microstructural modelling' Mechanics of Materials 32(8): 449-462.

Vaughan T. Micromechanical Modelling of Damage and Failure in Fibre Reinforced Composites under Loading in the Transverse Plane. PhD Thesis, Limerick: University of Limerick; 2011.

Canal, L. P., J. Segurado and J. Llorca (2009). 'Failure surface of epoxy-modified fiber-reinforced composites under transverse tension and out-of-plane shear' International Journal of Solids and Structures 46(11-12): 2265-2274.

González, C. and J. Llorca (2007). 'Mechanical behavior of unidirectional fiber-reinforced polymers under transverse compression: Microscopic mechanisms and modeling' Composites Science and Technology 67(13): 2795-2806.

Totry, E., C. González and J. Llorca (2008a). 'Failure locus of fiber-reinforced composites under transverse compression and out-of-plane shear' Composites Science and Technology 68(3-4): 829-839.